A. Shahnazarian, and various students (Univ. of Cologne) for their help in core processing and to T. Matrosova for contributing modern surface pollen data. Thanks to A. Dolan for supplying PlioMIP model output and I. Castañeda for discussions and help with figures. The data reported in this paper are archived in the databases of PANGAEA (doi:10.1594/PANGAEA.808834) and the U.S. National Geophysical Data Center (ftp://ftp.ncdc.noaa.gov/pub/data/paleo/paleolimnology/asia/russia/elgygytgyn2013.xls).

**Supplementary Materials**
www.sciencemag.org/cgi/content/full/science.1233137/DC1
Materials and Methods
Supplementary Text
Figs. S1 to S9
Tables S1 to S5
References (*64*–*105*)

23 November 2012; accepted 24 April 2013
Published online 9 May 2013;
10.1126/science.1233137



# Massive Dirac Fermions and Hofstadter Butterfly in a van der Waals Heterostructure

B. Hunt,[1]* J. D. Sanchez-Yamagishi,[1]* A. F. Young,[1]* M. Yankowitz,[2] B. J. LeRoy,[2] K. Watanabe,[3] T. Taniguchi,[3] P. Moon,[4]† M. Koshino,[4] P. Jarillo-Herrero,[1]‡ R. C. Ashoori[1]‡

van der Waals heterostructures constitute a new class of artificial materials formed by stacking atomically thin planar crystals. We demonstrated band structure engineering in a van der Waals heterostructure composed of a monolayer graphene flake coupled to a rotationally aligned hexagonal boron nitride substrate. The spatially varying interlayer atomic registry results in both a local breaking of the carbon sublattice symmetry and a long-range moiré superlattice potential in the graphene. In our samples, this interplay between short- and long-wavelength effects resulted in a band structure described by isolated superlattice minibands and an unexpectedly large band gap at charge neutrality. This picture is confirmed by our observation of fractional quantum Hall states at $\pm^5/_3$ filling and features associated with the Hofstadter butterfly at ultrahigh magnetic fields.

The ability to tailor the properties of electronic devices is one of the landmark achievements of modern technology and motivates a sizable fraction of modern research in condensed matter physics. Just as crystal structure can determine the electronic properties of a material, artificial periodic superstructures can be used to modify the electronic band structure of existing materials (*1*). The band structure of pristine graphene consists of linearly dispersing energy bands, which touch at two degenerate "Dirac points." This degeneracy is protected by the equivalence of the A and B triangular sublattices that make up the graphene honeycomb (*2*) and is responsible for graphene's semimetallic behavior. Theory suggests that the electronic properties of graphene can be tuned via external periodic potentials: Long-wavelength superlattices have been predicted to lead to the formation of additional gapless Dirac points at finite energy (*3*), whereas atomic-scale modulations, by breaking the A-B sublattice symmetry, may turn graphene from a semimetal into a semiconductor (*4*). Experimental efforts to make high-mobility functional devices based on band structure engineering, however, have been hindered by growth and nanofabrication limitations (*5*).

Recently, a new approach has become available through the use of hexagonal boron nitride (hBN) as a planar crystalline substrate. hBN is isostructural to graphene but has boron and nitrogen atoms on the A and B sublattices, leading to a large band gap (*6*). The weak interlayer van der Waals forces in both graphene and hBN permit the fabrication of multilayer heterostructures by sequential transfer of individual layers (*7*). During the transfer process, the angular alignment of the constituent crystals (θ) can in principle be controlled, but the graphene and hBN lattices retain their natural 1.8% mismatch (*4*). The frequency difference of the mismatched lattices leads to the formation of a moiré pattern with wavelength λ(θ) that can be much larger than the lattice constant (*8*, *9*) (Fig. 1A).

The effect of the moiré on the graphene electronic structure can be decomposed into two parts (*10*). The moiré pattern results in a λ-scale modulation of the graphene-hBN coupling, forming a smooth superlattice potential. More subtly, the moiré also modulates the local asymmetry

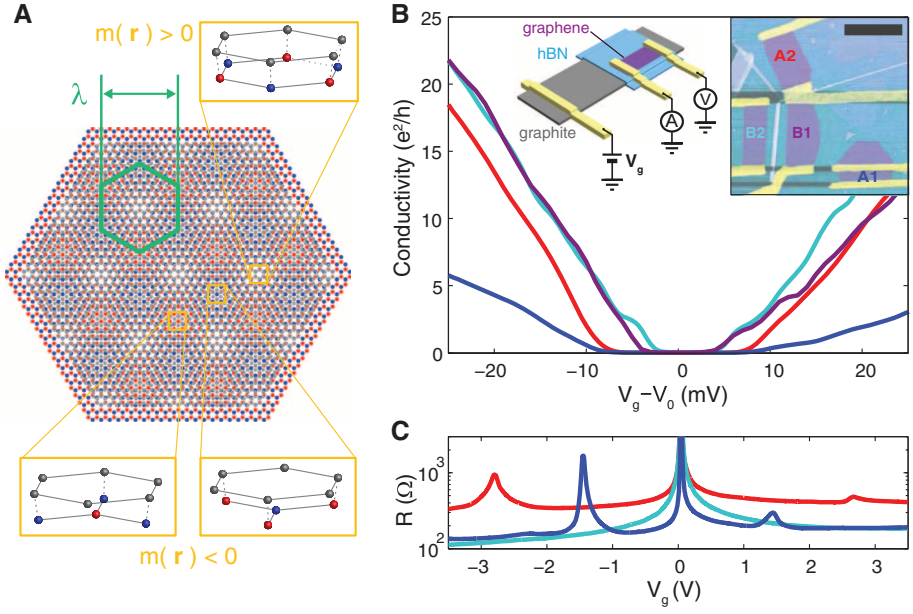


**Fig. 1. Insulating states and superlattice minibands in a graphene-hBN heterostructure.** (**A**) Schematic of the moiré pattern for graphene (gray) on hBN (red and blue), for zero misalignment angle and an exaggerated lattice mismatch of ~10%. The moiré unit cell is outlined in green. Regions of local quasi-epitaxial alignment lead to opposite signs of the sublattice asymmetry, $m(\mathbf{r})$, in different regions (gray, carbon; red, boron; blue, nitrogen). (**B**) Low-temperature ($T$ = 150 mK) conductivity near charge neutrality of four heterostructure devices (A1, A2, B1, and B2). The CNP offset $V_0$ = 37, 37, 46, and 42 mV, respectively. Left inset: Measurement schematic. Right inset: False-color atomic force microscopy image. Scale bar, 3 μm. (**C**) Resistance over a larger gate range. Finite-density resistance peaks indicate full filling of the lowest superlattice miniband in two of the four measured devices (A1 and A2) within the experimentally accessible density range.

[1]Department of Physics, Massachusetts Institute of Technology, Cambridge, MA 02139, USA. [2]Department of Physics, University of Arizona, Tucson, AZ 85721, USA. [3]Advanced Materials Laboratory, National Institute for Materials Science, Tsukuba, Ibaraki 305-0044, Japan. [4]Department of Physics, Tohoku University, Sendai 980-8578, Japan.

*These authors contributed equally to this work.
†Present address: Korea Institute for Advanced Study, Seoul 130-722, Republic of Korea.
‡Corresponding author. E-mail: pjarillo@mit.edu (P.J.-H.); ashoori@mit.edu (R.C.A.)

Downloaded from http://science.sciencemag.org/ on April 19, 2017

between the graphene sublattices induced by the difference in potential between boron and nitrogen atoms in the hBN. The resulting A-B potential difference in the graphene, parameterized in Fig. 1A as $m(\mathbf{r})$, oscillates across the superlattice unit cell (*11*), leading to nearly complete cancellation (*10*) upon spatial averaging. As we demonstrate, however, the absence of sublattice symmetry nonetheless has considerable experimental consequences for the electronic properties near the charge neutrality point.

We present measurements of four heterostructure devices consisting of a monolayer graphene flake on a 7-nm-thick hBN substrate (*9*), which itself sits on top of a graphite local gate (Fig. 1B). The proximal gate electrode serves both as an extremely flat substrate and to screen long-range potential fluctuations in the graphene (*12*), leading to high-quality devices with field-effect mobilities of ~100,000 $cm^2 V^{-1} s^{-1}$ and well-quantized quantum Hall plateaus at fields $B < \sim 100$ mT (*9*). In contrast to the majority of graphene devices—which, with few exceptions (*12*, *13*), are semimetallic with zero-field minimum conductivity of $\sim 2e^2/h$ (where $e$ is the electron charge and $h$ is Planck's constant)—all four devices are strongly insulating near the overall charge neutrality point (CNP) (Fig. 1B). In addition, two devices show pronounced resistance peaks at finite density (Fig. 1C), situated symmetrically about the CNP. Notably, the devices showing additional resistance peaks also have the strongest insulating states.

We ascribe the satellite resistance peaks to the Bragg scattering of charge carriers by the superlattice when the lowest electron and hole minibands are fully occupied (*8*, *14*–*16*). In graphene, as a consequence of the spin and valley degeneracies, full filling occurs at a density of four electrons per superlattice unit cell, $n = 4n_0$, where $1/n_0 = \sqrt{3}\lambda^2/2$ is the unit cell area (Fig. 1A). Using the density at which the peaks are observed for devices A1 and A2, we estimate $\lambda_{A1} = 11$ to 13.5 nm and $\lambda_{A2} = 7.5$ to 9.5 nm, where the error is dominated by uncertainty in the value of the hBN dielectric constant (*9*). Such large values of λ, not much smaller than the theoretical maximum of 14 nm, imply nearly perfect rotational alignment of the graphene and hBN, with $\theta < 2°$ for the two devices showing satellite peaks. Although we did not observe satellite peaks in devices B1 and B2, scanning tunneling topography measurements revealed moiré patterns with $\lambda_{B1} = 3.8$ nm and $\lambda_{B2} = 3.5$ nm (*9*), corresponding to close alignment with $\theta \approx 4°$.

The moiré pattern offers a unique opportunity to study the elementary problem of a charged quantum particle moving under the simultaneous

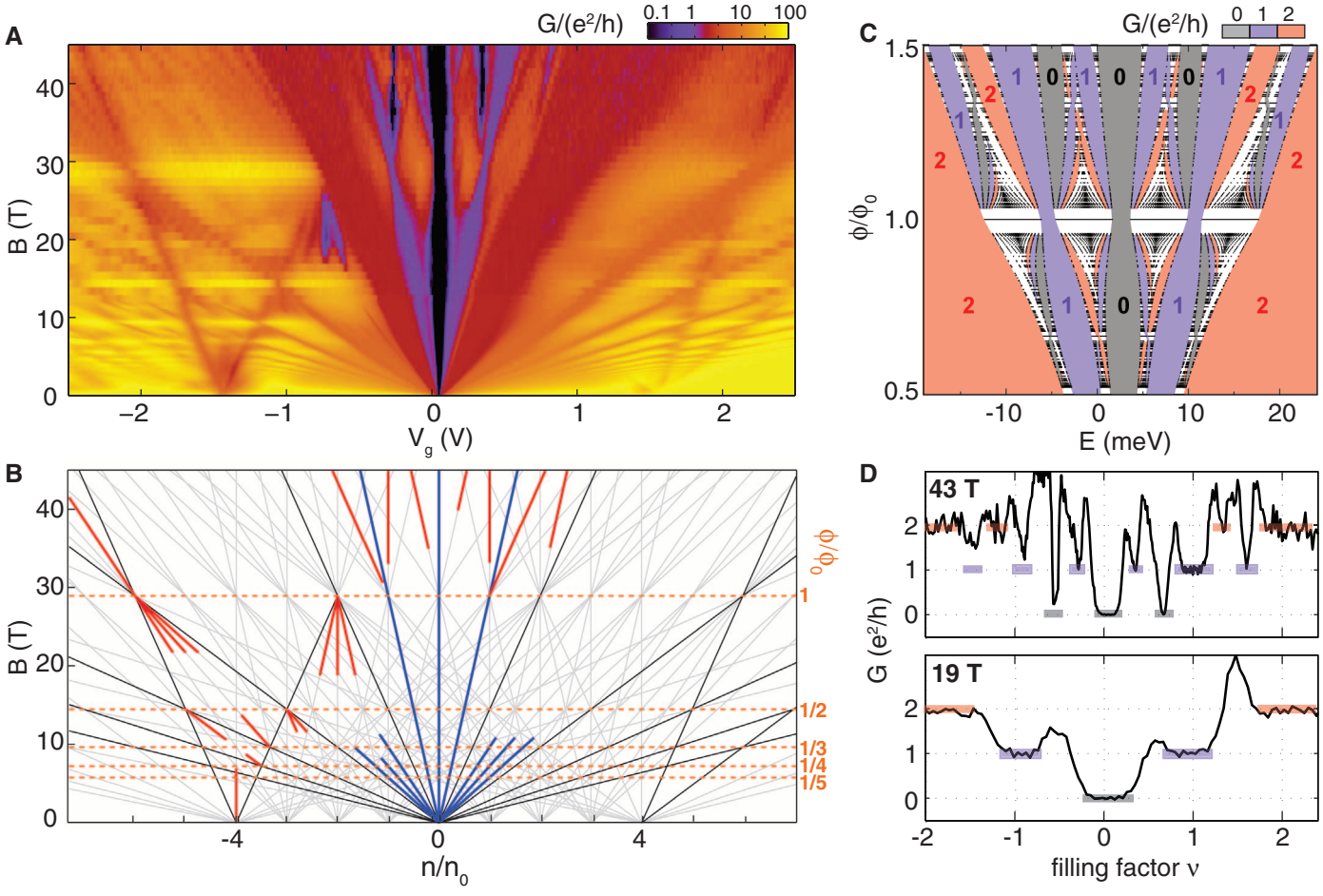


**Fig. 2. Hofstadter butterfly.** (**A**) Two-terminal magnetoconductance of device A1 up to 45 T. (**B**) In Wannier's theory (*21*), energy gaps in the Hofstadter spectrum are confined to linear trajectories $\phi/\phi_0 = (n/n_0 - s)/t$, where $s$ and $t$ are integers denoting the superlattice miniband filling index (*33*) and quantized Hall conductance of the gapped state, respectively. Gray lines indicate gaps for $-4 \le s \le 4$, with colored overlays indicating features observed in (A). Black, gaps requiring no broken symmetry; blue, broken-symmetry states for the central Landau fan; red, broken-symmetry states belonging to superlattice ($s \neq 0$) Landau fans. Gaps intersect at $\phi/\phi_0 = 1/q$, where $q$ is an integer (orange); $\phi = \phi_0$ at 29 T. (**C**) Theoretical Hofstadter energy spectrum for the fully spin- and sublattice-split $N = 0$ Landau level (*9*, *34*). Black points indicate regions of dense energy bands; intervening spectral gaps are color-coded to the associated two-terminal conductance $G = 2$ (red), 1 (purple), and 0 (gray) in units of $e^2/h$. (**D**) Conductance traces within the $N = 0$ Landau level at $B = 43$ T (top) and $B = 19$ T (bottom). Shaded rectangles are color-coded to the expected two-terminal conductance from the Hofstadter model of (C). The emergence of Hofstadter minigaps, characterized by a nonmonotonic sequence of quantized conductance plateaus, is evident in the 43 T data, where $\phi > \phi_0$. At 19 T, the quantum Hall sequence is the standard monotonic $G = |\nu|e^2/h$. Peaks between plateaus are due to diffusive transport in this wide–aspect ratio device.

Downloaded from http://science.sciencemag.org/ on April 19, 2017

influence of a periodic potential and a magnetic field (*17*–*20*) in the normally inaccessible regime of more than one magnetic flux quantum ($\phi_0$) per superlattice unit cell. In the absence of the superlattice, graphene is described at high fields by a set of discrete, highly degenerate Landau levels indexed by an integer $N$. The periodic potential splits the flat Landau level bands into "Hofstadter minibands" separated by a hierarchy of self-similar minigaps (*18*). Despite the intricate structure of the Hofstadter spectrum, the densities corresponding to the fractal minigaps follow simple linear trajectories as a function of magnetic field (*21*). Magnetoresistance data indeed show strong effects of the superlattice (Fig. 2A), including Landau fans originating from both the central and satellite zero-field resistance peaks. As recently demonstrated, the intersections between the central and satellite fans occur at $\phi = \phi_0/q$ (Fig. 2B), where $\phi$ is the magnetic flux per superlattice unit cell and $q$ is a positive integer (*15*, *16*). These intersections allow a second, independent method of measuring the unit cell area without reference to electrostatic parameters (*9*), giving $\lambda_{A1} = 12.9 \pm 0.2$ nm and $\lambda_{A2} = 9.2 \pm 0.1$ nm.

The full development of the Hofstadter butterfly, however, is most obvious in the regime $\phi/\phi_0 > 1$, which is challenging to access in monolayer graphene. Figure 2D shows the conductance within the $N = 0$ Landau level for two values of field corresponding to $\phi < \phi_0$ and $\phi > \phi_0$. At the higher field, the $N = 0$ Landau level is completely reconstructed, with a nonmonotonic sequence of conductance plateaus well-matched by tight binding calculations (*9*) of the Hofstadter butterfly spectrum in which phenomenological spin and sublattice symmetry-breaking terms have been included (Fig. 2C). The emergence of states with integer quantized conductance at noninteger filling of a single Landau level, severing the canonical relationship between quantized conductance and filling fraction, is the signature of the Hofstadter butterfly.

Equating the effect of the hBN substrate with that of a smooth superlattice potential explains many features of the experimental data, including the satellite resistance peaks and most features of the ultrahigh-$B$ transport data. However, this fails to account for the insulating state observed at charge neutrality, which persists uninterrupted from $B = 0$ to 45 T. To further explore the properties of this state, we used a low-temperature capacitance bridge to measure the capacitance of the graphene to the proximal graphite back gate (*9*, *22*). Capacitance measurements probe the thermodynamic density of states, $\partial n/\partial\mu$; for our parallel plate geometry, the measured capacitance $C_{meas}^{-1} = C_{geom}^{-1} + (Ae^2\partial n/\partial\mu)^{-1}$, where $C_{geom}$ is the geometric capacitance and $A$ is the sample area (*23*). Figure 3A shows magnetocapacitance data from a typical, semimetallic graphene-on-hBN device. The capacitance, and by extension the density of states, has a minimum at charge neutrality. As the field is increased, this minimum is replaced by a local maximum, signifying the formation of the zero-energy Landau level characteristic of massless Dirac fermions (*24*). Capacitance measurements of an insulating graphene device reveal very different behavior (Fig. 3B). No peak forms at the CNP at finite field, as can be seen from the dark vertical region centered at gate voltage $V_g = 41$ mV, indicating that the $N = 0$ Landau level is split into two finite-energy sublevels; in other words, a Landau level never forms at zero energy.

As we increase the field further (Fig. 3C), additional minima in capacitance appear at all integer filling factors $\nu$—including those not belonging to the standard monolayer graphene sequence—indicating the emergence of exchange-driven broken-symmetry states (*25*). Capacitance minima associated with fractional quantum Hall states appear (Fig. 3D) at all multiples of ⅓ for $-2 < \nu < 2$. Notably, this sequence includes robust features at $\nu = \pm 5/3$ not observed in previous studies (*26*, *27*) of semimetallic monolayer graphene. These states are thought to be described by a fully spin- and sublattice-polarized Laughlin wave function (*28*, *29*); their absence in semimetallic graphene is attributed (*26*, *30*) to the low energy cost of exciting charge carriers to the unoccupied, energetically equivalent sublattice. Our observation of the $\pm 5/3$ states suggests that sublattice symmetry is broken in our graphene-hBN heterostructures.

In the Dirac equation description of graphene, sublattice symmetry breaking can be parameterized by a mass. In our heterostructures, this mass term $m(\mathbf{r})$ is expected to oscillate across the moiré unit cell (Fig. 1A). Notably, the low-density phenomenology of our insulating graphene at low fields ($\phi << \phi_0$)—including the insulating gap, the absence of a zero-energy Landau level, and the observation of the $\nu = \pm 5/3$ states—can be captured by a Dirac equation with a spatially uniform global effective mass, $m^*$. The resulting Hamiltonian describing physics in the vicinity of the $K$ ($K'$) point is

$$\hat{H} = v_F \boldsymbol{\sigma}\cdot\mathbf{p} + m^* v_F^2 \hat{\sigma}_z = \begin{pmatrix} \pm m^* v_F^2 & v_F(p_x - ip_y) \\ v_F(p_x + ip_y) & \mp m^* v_F^2 \end{pmatrix} \quad (1)$$

where $v_F$ is the Fermi velocity, $\mathbf{p} = (p_x, p_y)$ is the momentum in the graphene plane, $\boldsymbol{\sigma} = (\sigma_x, \sigma_y)$,

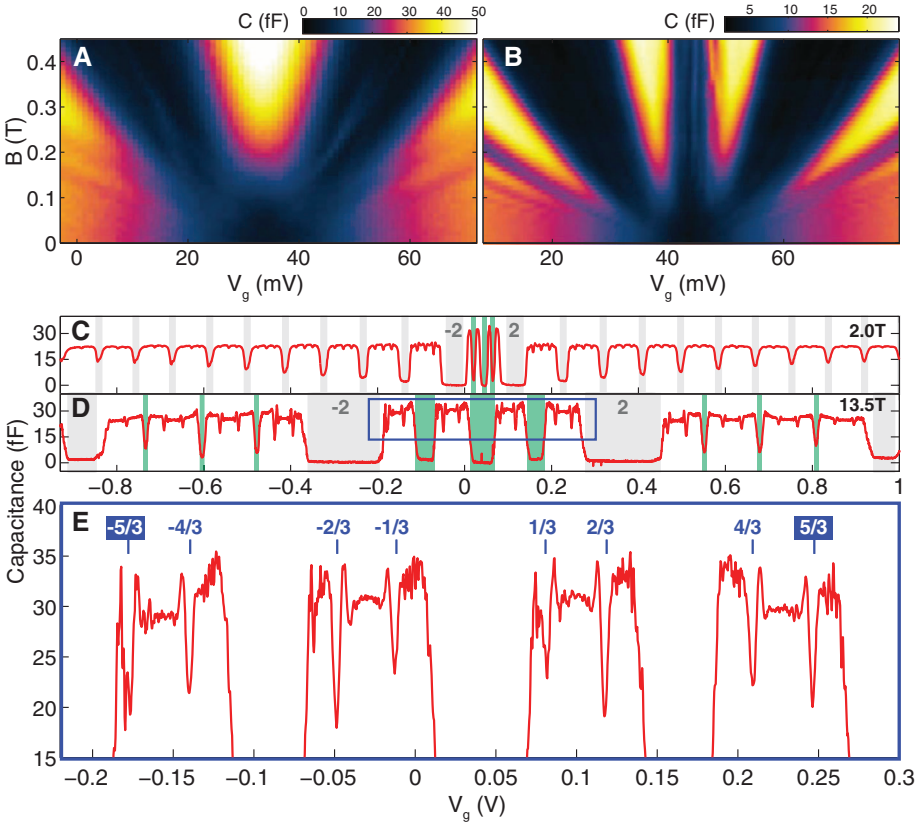


**Fig. 3. Magnetocapacitance of semimetallic and insulating graphene devices.** (**A**) Capacitance of a typical semimetallic graphene device. The zero-energy Landau level forms at ~0.15 T, appearing as a local maximum at the CNP ($V_g = 34.5$ mV). (**B**) Capacitance of an insulating graphene device (B2) under similar conditions. In contrast to (A), the density of states is at a local minimum for all fields at charge neutrality ($V_g = 44$ mV). (**C** and **D**) Capacitance of device B2 at $B = 2.0$ T (C) and 13.5 T (D). Cyclotron gaps are shaded gray ($\nu = \pm 2$ labeled) and broken-symmetry gaps are shaded green. (**E**) Fractional quantum Hall (FQH) states in the $N = 0$ Landau level. The incompressible features at $\nu = \pm 5/3$ are of similar strength to the other FQH states.

Downloaded from http://science.sciencemag.org/ on April 19, 2017

and the Pauli matrices $\{\sigma_i\}$ operate in the basis of the two sublattices. The resulting energy spectrum at zero magnetic field,

$$E(\mathbf{p}) = \pm\sqrt{v_F^2|\mathbf{p}|^2 + (m^* v_F^2)^2} \quad (2)$$

features a band gap $\Delta = 2m^* v_F^2$ at charge neutrality. In a quantizing magnetic field, the Landau level spectrum is given by

$$E_N = \pm\sqrt{2(\hbar v_F)^2|N|/\ell_B^2 + (m^* v_F^2)^2} \quad (3)$$

where $\hbar = h/2\pi$ and $\ell_B = \sqrt{\hbar/(eB)}$ is the magnetic length (*9*). The mass term does not lift the Landau level degeneracy for $|N| > 0$; this is reflected in our data (Fig. 3C) by the observation of symmetry breaking in the higher Landau levels only at higher magnetic fields, presumably due to exchange interactions, as in semimetallic graphene (*25*). However, the splitting of the $N = 0$ Landau level into two sublattice-polarized branches at $E_0 = \pm m^* v_F^2$ is consistent with the persistent gap at charge neutrality, as well as the observation of the $\pm^5/_3$ fractional quantum Hall states.

The observation of band gaps in samples with long-wavelength moiré patterns is not likely to be coincidental. Naïvely, $m(\mathbf{r})$ nearly vanishes upon spatial average, calling into question whether a mismatched hBN substrate can open a measurable gap. Indeed, predictions for how the global parameter $m^*$ depends on the microscopic structure of $m(\mathbf{r})$ vary by several orders of magnitude depending on theoretical assumptions (*4*, *10*, *31*, *32*). To quantitatively assess the connection between $\lambda$ and $m^*$, we measured the band gap using the temperature dependence of the charge-neutrality point conductvity (Fig. 4, A and B) and independently measured the width in gate voltage of the insulating state, which places an upper bound on the chemical potential difference across the band gap (*9*). Figure 4C shows a correlation between moiré wavelength and the measured gaps, which suggests that the interaction of the graphene flake with the closely aligned hBN substrate is responsible for the insulating behavior. Single-particle theories of graphene on hBN (*10*, *31*) predict $\Delta \approx 5$ to 10 meV for zero misalignment angle, for which the gap is expected to be maximal. Our measured band gaps exceed these predictions even for nonzero twist. In addition, the discrepancy between the two methods for gap determination implies that $\Delta$ depends on chemical potential, suggesting that many-body interactions may play a role in enhancing $\Delta$ (*32*). However, quantitative comparison with the predicted power-law dependence of $\Delta(\lambda)$ will require more extensive data.

The ability to engineer a nonzero band mass in graphene has far-reaching implications for future experimental efforts. The possibility of an alignment-dependent mass may require a reinterpretation of experiments involving graphene-hBN heterostructures, even as it engenders new opportunities for the design of electronic devices. The gapped spectrum and the tunability of the associated effective mass provide a useful tool in nanoengineering based on electrostatic confinement, as well as a new design parameter in the study of many-body effects in monolayer graphene.

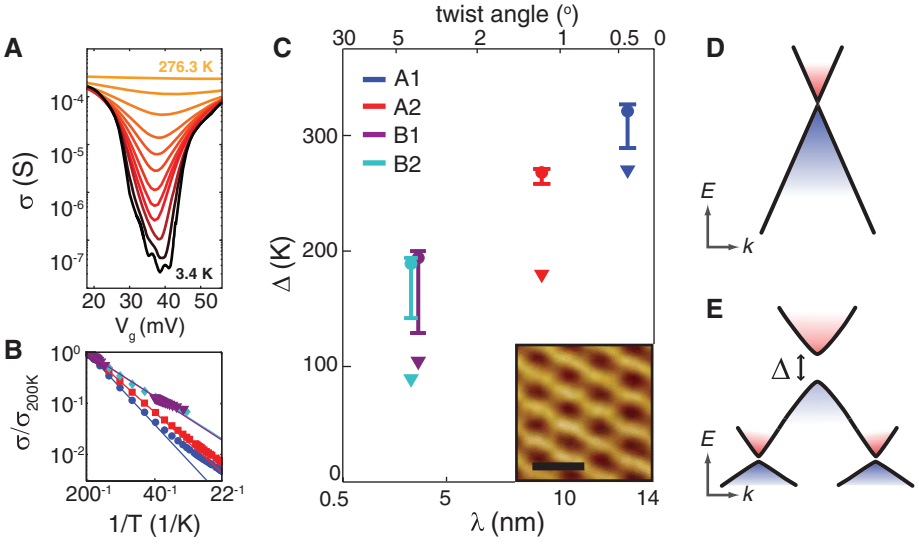


**Fig. 4. Energy gaps of the zero-field insulator.** (**A**) Conductivity of the insulator device A1 at a series of temperatures. (**B**) Arrhenius plot of $\sigma_{CNP}$ for all four devices. Lines are fits to the simply activated form $\sigma_{CNP}(T) \propto \exp(-\Delta/2T)$, giving $\Delta_{A1} = 321$ K, $\Delta_{A2} = 268$ K, $\Delta_{B1} = 194$ K, and $\Delta_{B2} = 189$ K. (**C**) Correlation of observed band gaps with moiré wavelength $\lambda$. Circles denote thermal activation gap (Fig. 2B); error bars are estimated from the uncertainty in the range of simply activated behavior. Inverted triangles denote width in gate voltage of the insulating state. $\lambda$ is extracted from the period of the Hofstadter oscillations for A1 and A2, and from STM measurements for B1 and B2. Inset: Scanning tunneling topography image of B2 (scale bar, 5 nm). (**D**) Schematic band structure for semimetallic graphene, showing the linear dependence of energy $E$ on two-dimensional wave vector $k = |\mathbf{p}|/\hbar$. (**E**) Schematic band structure for an insulating graphene-hBN heterostructure, showing the band gap and moiré minibands.


**References and Notes**

1. R. Tsu, *Superlattice to Nanoelectronics* (Elsevier, London, 2010).
2. P. R. Wallace, *Phys. Rev.* **71**, 622 (1947).
3. C.-H. Park *et al.*, *Phys. Rev. Lett.* **101**, 126804 (2008).
4. G. Giovannetti, P. A. Khomyakov, G. Brocks, P. J. Kelly, J. van den Brink, *Phys. Rev. B* **76**, 073103 (2007).
5. F. Schwierz, *Nat. Nanotechnol.* **5**, 487 (2010).
6. Y. Kubota, K. Watanabe, O. Tsuda, T. Taniguchi, *Science* **317**, 932 (2007).
7. C. R. Dean *et al.*, *Nat. Nanotechnol.* **5**, 722 (2010).
8. M. Yankowitz *et al.*, *Nat. Phys.* **8**, 382 (2012).
9. See supplementary materials on *Science* Online.
10. M. Kindermann, B. Uchoa, D. L. Miller, *Phys. Rev. B* **86**, 115415 (2012).
11. D. L. Miller *et al.*, *Nat. Phys.* **6**, 811 (2010).
12. L. A. Ponomarenko *et al.*, *Nat. Phys.* **7**, 958 (2011).
13. F. Amet, J. R. Williams, K. Watanabe, T. Taniguchi, D. Goldhaber-Gordon, *Phys. Rev. Lett.* **110**, 216601 (2013).
14. J. R. Wallbank, A. A. Patel, M. Mucha-Kruczynski, A. K. Geim, V. I. Fal'ko, *Phys. Rev. B* **87**, 245408 (2013).
15. C. R. Dean *et al.*, *Nature* **497**, 598 (2013).
16. L. A. Ponomarenko *et al.*, *Nature* **497**, 594 (2013).
17. M. Y. Azbel, *Sov. Phys. JETP* **19**, 634 (1964).
18. D. R. Hofstadter, *Phys. Rev. B* **14**, 2239 (1976).
19. T. Schlösser, K. Ensslin, J. P. Kotthaus, M. Holland, *Semicond. Sci. Technol.* **11**, 1582 (1996).
20. C. Albrecht *et al.*, *Phys. Rev. Lett.* **86**, 147 (2001).
21. G. H. Wannier, *Phys. Stat. Sol. B* **88**, 757 (1978).
22. R. C. Ashoori *et al.*, *Phys. Rev. Lett.* **68**, 3088 (1992).
23. S. Luryi, *Appl. Phys. Lett.* **52**, 501 (1988).
24. A. K. Geim, K. S. Novoselov, *Nat. Mater.* **6**, 183 (2007).
25. A. F. Young *et al.*, *Nat. Phys.* **8**, 550 (2012).
26. C. R. Dean *et al.*, *Nat. Phys.* **7**, 693 (2011).
27. B. E. Feldman, B. Krauss, J. H. Smet, A. Yacoby, *Science* **337**, 1196 (2012).
28. C. Tőke, P. E. Lammert, V. H. Crespi, J. K. Jain, *Phys. Rev. B* **74**, 235417 (2006).
29. V. M. Apalkov, T. Chakraborty, *Phys. Rev. Lett.* **97**, 126801 (2006).
30. N. Shibata, K. Nomura, *Phys. Rev. B* **77**, 235426 (2008).
31. B. Sachs, T. O. Wehling, M. I. Katsnelson, A. I. Lichtenstein, *Phys. Rev. B* **84**, 195414 (2011).
32. J. C. W. Song, A. V. Shytov, L. S. Levitov, http://arxiv.org/abs/1212.6759 (2012).
33. A. H. MacDonald, *Phys. Rev. B* **28**, 6713 (1983).
34. M. Koshino, T. Ando, *Phys. Rev. B* **73**, 155304 (2006).



**Acknowledgments:** We acknowledge helpful discussions with C. Dean, H. Churchill, L. Levitov, and J. Song. B.H. and R.C.A. were funded by the Basic Energy Sciences Program, Office of Science, U.S. Department of Energy (DOE), contract FG02-08ER46514, and by Gordon and Betty Moore Foundation grant GBMF2931. J.D.S.-Y. and P.J.-H. were primarily supported by the DOE Office of Basic Energy Sciences, Division of Materials Sciences and Engineering under grant DE-SC0001819. Early fabrication feasibility studies were supported by NSF Career Award DMR-0845287 and the ONR GATE MURI. M.Y. and B.J.L. were supported by NSF grant EECS-0925152. This work made use of the MRSEC Shared Experimental Facilities supported by NSF under grant DMR-0819762 and of Harvard's CNS, supported by NSF under grant ECS-0335765. Some measurements were performed at the National High Magnetic Field Laboratory, which is supported by NSF Cooperative Agreement DMR-0654118, the State of Florida, and DOE. A.F.Y. acknowledges the support of the Pappalardo Fellowship in Physics. M.K. was supported by Japan Society for the Promotion of Science (JSPS) Grant-in-Aid for Scientific Research 24740193; P.M. was supported by JSPS Grant-in-Aid for Research Activity Start-up (grant 23840004).


**Supplementary Materials**

www.sciencemag.org/cgi/content/full/science.1237240/DC1
Materials and Methods
Supplementary Text
Figs. S1 to S18
References (*35*–*45*)


1 March 2013; accepted 8 May 2013
Published online 16 May 2013;
10.1126/science.1237240


Downloaded from http://science.sciencemag.org/ on April 19, 2017

**Massive Dirac Fermions and Hofstadter Butterfly in a van der Waals Heterostructure**
B. Hunt, J. D. Sanchez-Yamagishi, A. F. Young, M. Yankowitz, B. J. LeRoy, K. Watanabe, T. Taniguchi, P. Moon, M. Koshino, P. Jarillo-Herrero and R. C. Ashoori (May 16, 2013)
*Science* **340** (6139), 1427-1430. [doi: 10.1126/science.1237240] originally published online May 16, 2013

Editor's Summary

**Graphene, Gapped and Butterflied**

The remarkable transport properties of graphene, such as the high electron mobility, make it a promising material for electronics. However, unlike semiconductors such as silicon, graphene's electronic structure lacks a band gap, and a transistor made out of graphene would not have an "off" state. **Hunt *et al.*** (p. 1427, published online 16 May; see the Perspective by **Fuhrer**) modulated the electronic properties of graphene by building a heterostructure consisting of a graphene flake resting on hexagonal boron nitride (hBN), which has the same honeycomb structure as graphene, but consists of alternating boron and nitrogen atoms instead of carbons. The natural mismatch between the graphene and hBN lattices led to a moire pattern with a large wavelength, causing the opening of a band gap, the formation of an elusive fractional quantum Hall state, and, at high magnetic fields, a fractal phenomenon in the electronic structure called the Hofstadter butterfly.

This copy is for your personal, non-commercial use only.

**Article Tools** Visit the online version of this article to access the personalization and article tools:
http://science.sciencemag.org/content/340/6139/1427

**Permissions** Obtain information about reproducing this article:
http://www.sciencemag.org/about/permissions.dtl

*Science* (print ISSN 0036-8075; online ISSN 1095-9203) is published weekly, except the last week in December, by the American Association for the Advancement of Science, 1200 New York Avenue NW, Washington, DC 20005. Copyright 2016 by the American Association for the Advancement of Science; all rights reserved. The title *Science* is a registered trademark of AAAS.

Downloaded from http://science.sciencemag.org/ on April 19, 2017